# A Continuous, Impedimetric Parylene Flow Sensor

Trevor Q. Hudson, *Student Member, IEEE*, and Ellis Meng, *Fellow, IEEE*

***Abstract*— A continuously recording, impedimetric thermal liquid flow sensor fabricated on a Parylene C thin film substrate is presented for the first time. The sensing concept, inspired by hot-film anemometry, includes an additional upstream unheated reference electrode pair which enabled attenuation of environmental drift in impedance by more than 5×. This sensor design and transduction approach was motivated by the need for an alternative to traditional hot-film anemometers for *in vivo* applications. An analytical model was developed to describe the axial fluid temperature surrounding the impedimetric sensor and its effect on solution conductivity. The impact of heater power was modeled and matched with experimental data; similar analysis was conducted for other parameters including channel height, ambient temperature, and electrolyte concentration. The sensor achieved a $2\sigma$ resolution of 17 $\mu$L/min over the range 43-200 $\mu$L/min. The models and fabricated device significantly expand our understanding of thermal impedimetric flow sensing. [2020-0357]**

***Index Terms*— Thermal flow sensor, anemometer, Parylene C, electrochemical impedance, simulation, implantable device.**

## I. Introduction

THERMAL flow meters measure fluid mass flow using at least one heating element and one temperature sensor. They are common in a variety of applications for their low cost, ease of manufacture, and simple operation.

These thermal sensors are distinguished by their measurement principle and specific layout [1]–[3]; here, the focus is on hot-wire or hot-film anemometers that measure heat transfer resulting from the interaction of fluid flow and a heating element.

Anemometric sensors were developed in the early 1900's, when the idea of using temperature changes in constantly-powered copper wires to measure wind velocity was put forward by Kennelly and others [4]–[6], and later expanded upon by King and Barnes [7]. Later, a microfabricated thermal flow sensor was developed by replacing the copper wire with a thin film resistive layer deposited on bulk silicon, then on isolated membranes and thin micro-bridges for improved thermal isolation [8]–[10]. Progress in this field continues with promising materials such as SiC [11] and temperature-sensitive fluorescent detection elements [12], and new geometries to control heat transfer [13], [14]. Thermal liquid flow sensors exist in a variety of flow rates, sensitivities, response times, and overheat temperatures to match their use cases.

Traditional materials used in these sensors are rigid which can enhance the odds and severity of the inflammatory foreign body response post-implantation [15]–[18]. Thermal flow sensors can instead be fabricated on flexible polymer substrates [19]–[22]. Polymers also have low thermal conductivities compared to silicon and glass, attenuating dissipative losses through substrate [23].

Most liquid thermal flow sensors require a barrier layer to electrically insulate their temperature sensor. This in turn necessitates relatively high power for sensitive operation. Local overheat temperatures are commonly 12 – 15 °C, though certain sensors require temperatures around 60 °C [24]. However, many tissues begin to suffer damage at 43 °C [25], suggesting overheat temperature for chronic implants should be kept below 6 °C. Additionally, ISO guidelines require exterior surfaces of an implantable device to be no greater than 2 °C over body temperature.

Flow sensors that detect changes in the solution electrochemical impedance (EI) between exposed electrodes can operate at lower temperatures [26]–[28]. Recently, an EI-based thermal flow sensor was demonstrated which exploits the high temperature coefficient of resistance (TCR) of ionic solution by using fluid between two exposed platinum electrodes as a highly-responsive temperature sensor [29]. This novel method obviates the need for sensor passivation, thus enabling a new class of flow sensor for chronic biological fluid monitoring.

To date, pseudo-time-of-flight [24] and calorimetric [30] EI-based sensors have been explored. Time-of-flight sensors measure the transit time of a thermal pulse to a downstream temperature sensor. Calorimeters detect asymmetry in the fluid temperature profile around the heater via upstream and downstream temperature sensors. In prior work, pulsed heater activation was used to minimize the effect of sensor drift and minimize overheat temperature to 1 °C. However, this strategy suffered from momentary interruptions of flow, required relatively complex circuitry to control timing and data analysis, and was restricted to discrete measurements.

Here, a continuous EI-based flow sensor and analytical model are presented. Continuous monitoring represents a significant advance from prior work, where proof-of-concept experimental results were presented [31]. By measuring the EI of fluid above a heater, an impedimetric analog of a hot-film anemometer is introduced. Flow sensing was performed using two separate dies, each having microfabricated

Manuscript received October 26, 2020; revised March 16, 2021; accepted March 17, 2021. Date of publication March 30, 2021; date of current version June 1, 2021. This work was supported in part by the National Science Foundation (NSF) under Award EFRI-1332394 and Award IIP-182773 and in part by the University of Southern California Andrew and Erna Viterbi Fellowship. Subject Editor K. Cheung. *(Corresponding author: Ellis Meng.)*

The authors are with the Department of Biomedical Engineering, University of Southern California, Los Angeles, CA 90089 USA (e-mail: tqhudson@usc.edu; ellis.meng@usc.edu).

Color versions of one or more figures in this article are available at https://doi.org/10.1109/JMEMS.2021.3067573.

Digital Object Identifier 10.1109/JMEMS.2021.3067573

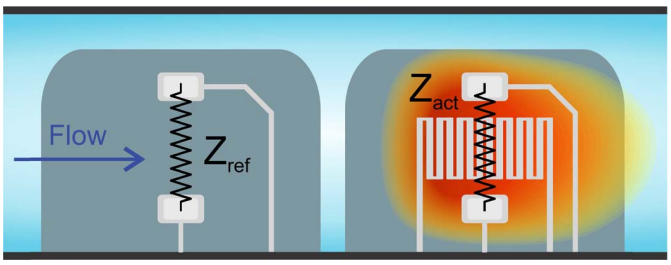


Fig. 1. Diagram of flow sensor operation. Impedance in the upstream reference cell is compared against the active cell to obtain stable tracking of flow rate.

EI temperature sensors, to acquire a differential signal resistant to common-mode impedance drift from temperature, solute-electrode adhesion, and solution ingress to sensor components. Analytical and finite element models were developed and facilitated understanding of sensor behavior. This new continuous EI sensor concept targets lower liquid flow rates for eventual use *in vivo* with comparable performance to existing pulsed EI sensors. The modeling and experimental data presented here are a significant advance in our understanding of thermal impedimetric flow sensing concepts and design.

## II. Design and Fabrication

### A. Sensor Design

The flow sensor layout consisting of two separate sensor dies is illustrated in Fig. 1. This approach leverages preliminary results from prior work which utilized only a single sensor die [24]. One die is designated the active cell and contains a heater and EI pair. The second is a reference cell, which is placed upstream of the active cell to avoid thermal interference from flow passing across the sensor. The passage of current through the resistive heater (serpentine trace) warms adjacent fluid via Joule heating. The overheat temperature is detected via the change in solution conductivity, which is sensitive to temperature [29]. Solution resistance is then transduced by measuring electrochemical impedance between a pair of exposed electrodes.

The heater has a trace width of 25 $\mu$m, nominal resistance of 400 $\Omega$, and total footprint of 400 $\times$ 900 $\mu m^2$. Measurement electrodes have exposed areas of 180 $\times$ 80 $\mu m^2$ (GSA $=$ $1.44 \times 10^4 \mu m^2$). Electrodes are placed above and below the heater (with respect to flow velocity) with a separation distance of 1 mm. Parylene was chosen as the substrate material because of its biocompatibility and strong barrier properties. Platinum was selected as the sensing material for its corrosion resistance, compatibility with micromachining techniques, and biocompatibility [32].

### B. Fabrication and Packaging

Sensor fabrication follows established micromachining processes for Parylene C [33] (Fig. 2a). First, 10 $\mu$m of Parylene C was deposited onto a silicon carrier wafer at 35 millitorr using the Gorham process (Labcoter 2, Specialty Coating Systems, Indianapolis, IN) [34]. Heaters, sensing electrodes, and contact pads were defined using a lift-off procedure by

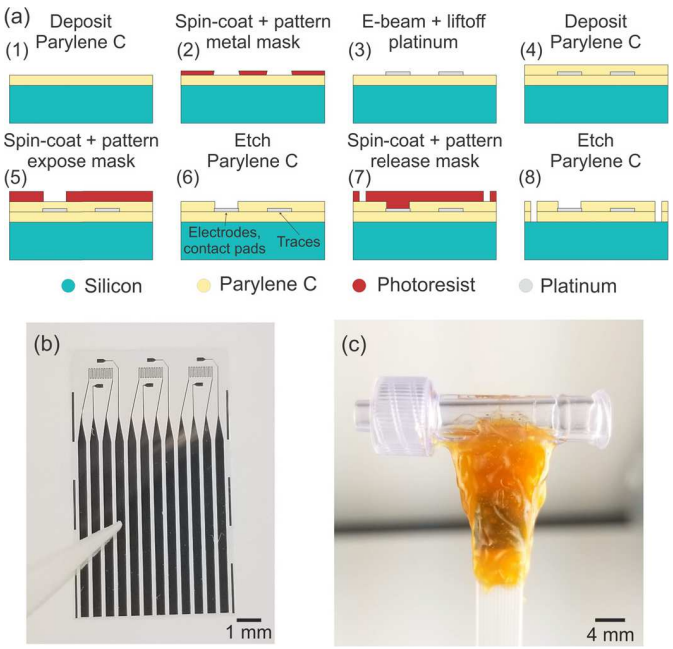


Fig. 2. (a) Flow sensor fabrication diagram. (b) Parylene die containing three flow sensors. (c) Packaged flow sensor.

electron-beam-deposition of 2000 Å of platinum (International Advanced Materials, North Charleston, SC) onto patterned AZ5214 photoresist (1.6 $\mu$m; Merck KGaA, Darmstadt, DE). A second 10 $\mu$m layer of Parylene C was deposited as an insulation layer. Then, electrodes and contact pads were exposed using a Bosch process-like oxygen-based deep reactive ion etch with AZ4620 (10 $\mu$m; Merck KGaA, Darmstadt, DE) photoresist as an etch mask [35]. Devices were released from the carrier silicon wafer (University Wafer, Boston, MA) by gently peeling while submerged in deionized water. Finally, devices were annealed at 200 °C for 48 hours under vacuum to increase adhesion between Parylene layers, reduce risk of delamination, and improve barrier properties [36].

Sensor packaging involved placing and sealing the sensor (Fig. 2b) into its flow chamber, electrically connecting its contact pads to measurement apparatus, and insulating sensor electronics from the fluid under test (Fig. 2c). To enable electrical contact, a ~180 $\mu$m (7 mil) thick polyetheretherketone backing was attached to the reverse side of the contact pad region to provide rigidity, allowing devices to be locked in a flip-lock zero insertion force connector in a solder-less packaging scheme [37]. Sensors were inserted into Luer-compatible modules (ID 3.25 mm)(80379, Qosina, Edgewood, NY) through 0.56 $\times$ 8 mm machined slits which allowed for easy integration into catheter systems currently used in the clinic. Biocompatible epoxy (EpoTek 353 ND-T, Epoxy Technology, Inc., Billerica, MA) was then used to pot contact pads and fluidically seal the sensor in the Luer module.

## III. Analytical Model

An analytical model of the thermal anemometer was developed using a one-dimensional lumped parameter approach to derive fluid temperature as a function of axial distance

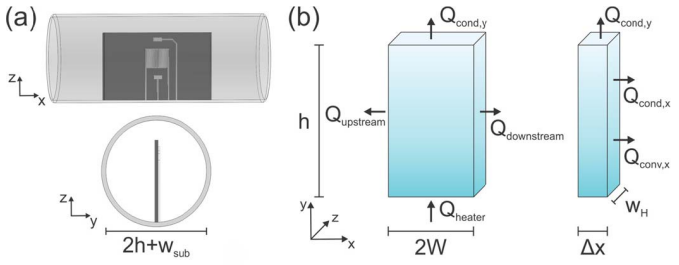


Fig. 3. (a) Rendering of a sensor cell packaged in the lumen of the Luer module as viewed from above the sensor (top) and through the module lumen (bottom). Module diameter is twice the channel height $h$ added to substrate width $w_{sub}$. (b) Volume slices of fluid located above heater (left) and upstream and downstream of the heater (right).

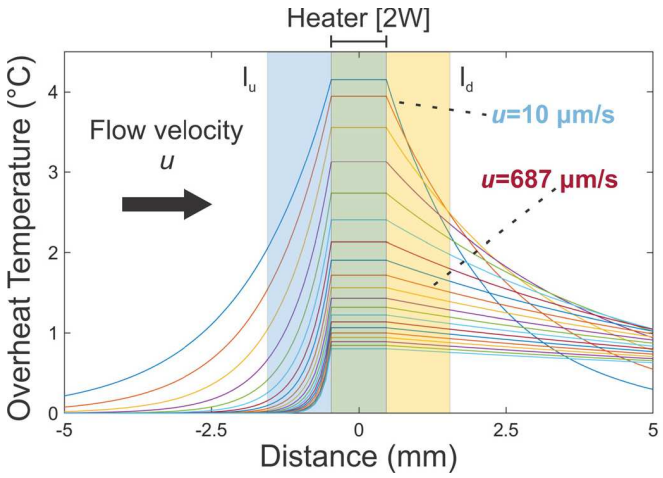


Fig. 4. Axial overheat temperature distribution of fluid along $x$ in the sensor lumen at 20 evenly spaced flow velocities from 10 – 1000 $\mu$m/s. The flow velocity corresponding to average adult cerebrospinal fluid production (687 $\mu$m/s) is highlighted as a reference for a physiologically relevant velocity. $l_u$ and $l_d$ define the upstream and downstream limits of the electroactive volume (see section III-C).

through the sensor. This mimics prior approaches used in microscale hot film anemometers [9], [38]–[40]. The corresponding change in solution resistivity of a fluid volume centered around the heater was derived and compared to experimental results.

### A. Fluid Temperature Distribution

The active cell of the sensor consists of a central heater flanked by two identical and equidistant exposed electrodes. The heater is energized at constant power so that energy is transferred into solution via Joule heating at a constant rate. Heat is removed by the adjacent solution primarily through conduction and convection. Given sufficient time and under steady flow, these competing effects result in a steady state temperature distribution in the local fluid which can be used to solve for flow velocity.

To determine the temperature distribution, the fluid volume adjacent to the sensor was divided into axial slices of infinitesimal thickness $\Delta x$ (Fig. 3). Fluid temperature was assumed to decrease from some $T_{absolute}$ to a minimum $T_{ambient}$ in the direction orthogonal to the substrate ($y$) and be constant over the sensor width ($z$). Through section III-A, $T$ refers to the overheat temperature $T_{absolute} - T_{ambient}$. The heat flux balance in any control volume is then:

$$Q_{cond,x} + Q_{conv,x} = Q_{cond,y} \tag{1}$$

where $Q_{cond,x}$ and $Q_{conv,x}$ represent heat transferred from adjacent volumes due to conduction and convection, respectively, and $Q_{cond,y}$ is heat lost to diffusion in $y$. Substrate conduction in Parylene C was disregarded due to its order-of-magnitude lower thermal conductivity compared to water (84 and 598 mW/(m·K), respectively). By adding expressions for these quantities as $\Delta x \to 0$, (1) becomes:

$$-\lambda \frac{T(x)}{2dx} w_H \bar{\delta} + \rho C_P u \frac{T(x)}{2} w_H \bar{\delta} = \lambda \frac{T(x)}{\bar{\delta}} w_H dx \tag{2}$$

where $\lambda$ is the thermal conductivity of fluid, $w_H$ is heater width in $z$, $\rho$ is the density of fluid, $C_P$ is the specific heat capacity of water, and $u$ is the flow velocity of fluid. $\bar{\delta}$ is the average height of the heated fluid layer in $y$, which we assume is equal to our channel height $h$ due to the very low flow rates in our system and consequent lack of a thermal boundary layer.

Equation (2) can then be rewritten as an ordinary differential equation:

$$\frac{1}{2}\frac{d^2T(x)}{dx^2} - \frac{u}{2\alpha}\frac{dT(x)}{dx} - \frac{k}{h^2}T(x) = 0 \tag{3}$$

where $\alpha$ is the thermal diffusivity of water. A correction coefficient $0 < k < 1$ was added to the $Q_{cond,y}$ term to model the reduced heat transfer capacity of the thermoplastic channel wall as compared to water at $y = \bar{\delta}$. After applying the boundary conditions $T(\pm W) = T_H$, $T(\pm\infty) = 0$, where $T_H$ is the temperature above the heater, the temperature distribution is:

$$T(x) = T_H e^{r_{1,2}(x \pm W)} \quad for\ x = (-\infty, -W) \cup (W, \infty)$$
$$r_{1,2} = \frac{uh \pm \sqrt{h^2u^2 + k8\alpha^2}}{2\alpha h} \tag{4}$$

To find $T_H$, the heat flux balance for the single control volume is:

$$Q_{heater} = Q_{cond,y} + Q_{upstream} + Q_{downstream} \tag{5}$$

or:

$$P = k\lambda 2W w_H / h\, T_H + \lambda (h w_H) r_1 T_H - \lambda (h w_H) r_2 T_H \tag{6}$$

where $P$ is the constant power dissipated by the heater. Solving this expression for temperature yields:

$$T(x) = T_H = \frac{hP}{\lambda w_H \left(k2W + h^2 (r_1 - r_2)\right)} \quad for\ x = [-W, W] \tag{7}$$

Temperature is plotted versus axial distance $x$ as a function of flow velocity $u$ (Fig. 4). $T$ is highest above the heater and decreases with distance $x$ in both directions. $T$ decreases more rapidly with distance in the upstream direction compared to downstream, especially at higher flows. This is caused by convective heating, or warm fluid being pushed downstream.

Similarly, $T$ and $\left|{}^{\partial T(x)}/_{\partial u}\right|$ are large at low flows, then diminish with larger values of $u$ due to convective cooling of $T_H$. At far downstream regions ($x \gg W$) however, temperature initially increases with $u$ due to convective heating then decreases as the drop in $T_H$ begins to dominate the response. For example, ${}^{\partial T(x)}/_{\partial u}$ is positive at $x = 5$ mm for the 5 lowest velocities, then negative after. This inflection point is the so-called "turnover velocity" described by Lammerink *et al.* [9] which would indicate the maximum useful range of a traditional resistive calorimeter at x = 5 mm. However, the impedimetric thermal anemometer will behave differently, as discussed below.

### B. Conductivity-Temperature Relation

Temperature transduction via the measurement of electrolyte conductivity is considered. Past work established that conductivity is temperature dependent [24], [29], but the causative mechanisms remain under investigation.

It is helpful to start with the behavior of ions at infinite dilution, or when their concentration approaches zero and interionic forces can be disregarded. Debye, Hückel, and Onsager established important limiting laws for ion transport and diffusion in this context based on the continuum model, which represents ions as hard spheres in an infinite dielectric medium [41]–[44]. While the limiting molar conductivity is a function of several variables such as temperature, pressure, and solvent identity, the effect of solute radius has been studied in the most detail, and in particular its nonmonotonic relationship with conductivity [45]–[54]. The effect of temperature has received much less attention from an analytical perspective.

Alternatively, it has been shown that the limiting molar conductivity $\Lambda_i^0$ of ion $i$ can be semiempirically linked to temperature and viscosity ($\eta$) of pure solvent via an Arrhenius relation:

$$\ln\left(\frac{\Lambda_i^0 \eta(T)}{10^{-4} S\ m\ mol^{-1} kgs^{-1}}\right) = A_i + {}^{B_i}/_{T} \tag{8}$$

where $A_i$ and $B_i$ are adjustable constants tabulated for individual ions [55]–[57]. The viscosity of pure water as a function of temperature can also be expressed empirically using an exponential fit [58].

An underlying motivation for the development of this impedimetric flow sensor is use with bodily fluids such as cerebrospinal fluid (CSF), which contains much lower amino acid, protein, and cell content compared with blood but similar electrolyte levels, rendering it isotonic with serum [59]. CSF has a total ionic strength of 148 mM, with sodium and chloride combined contributing ~88% of the total osmolarity and the remainder from bicarbonate and other more dilute ions [60]. For simplicity, only the limiting molar conductivities of sodium and chloride were considered. It is possible to use more complex methods to account for all ions for additional accuracy [55], [61].

At limiting ionic concentrations, Kohlrausch's law states that the equivalent conductivity can be obtained by simply summing the contributions from each individual species [57]. Practically, interionic interactions decrease molar solution conductivity at concentrations above ~1 mM.

Bernard and Turq *et al.* presented a convincing model for electrolyte mixtures [62], [63] using the mean spherical approximation (MSA) [64] in the continuum model. This method enables relatively simple and accurate analytical expressions for conductivity values up to molar concentrations. The MSA model uses the following general solution for the equivalent molar conductivity $\Lambda_i$ of an ion $i$ which is dissociated from a 1:1 electrolyte:

$$\Lambda_i = \Lambda_i^0 \left(1 + \frac{\delta \nu_i^{el}}{\nu_i^0}\right)\left(1 + \frac{\delta X}{X}\right) \tag{9}$$

where $\frac{\delta \nu_i^{el}}{\nu_i^0}$ is a correction factor due to electrophoretic effects and $\frac{\delta X}{X}$ for dielectric relaxation effects. These correction factors are functions of the valence, radii, concentration, and diffusion coefficient of the solute, and the viscosity, relative permittivity, and temperature of the solvent. Exact expressions are given in the appendix. Since a majority of the parameters are functions of temperature, the total equivalent conductivity of a given solution must be recalculated for any temperature change.

### C. Conductivity Weighting and Apparent Impedance

The closed-form analytical expressions for both solution temperature as a function of distance and flow velocity from (4) and (7), and solution conductivity of CSF as a function of temperature from (8) and (9), are now established. Returning to the geometric sensor model, the transducer consists of two electrodes which pass current through solution (see Fig. 1). The affected volume of fluid, or electro-active volume (EAV), is therefore the sample volume of the sensor.

However, varying current density throughout the electrolyte means that precisely defining the EAV is problematic, and implies that not all regions of the EAV will contribute equally to temperature sensing. For example, high current density near the sensing electrodes suggests fluid over the heater will dominate the overall response. Additionally, more current should flow through the low resistivity (high temperature) regions, further concentrating current density near the heater and causing a downstream skew as flow rate increases.

These effects can be accounted for by using weighted averages. First, reasonable functions for the temperature and current distributions must be created. Finite element analysis (see section V) yielded plots of temperature and current density distribution in $y$, which were approximated using polynomial regression (Fig. 5). The one-dimensional current density-weighted temperature average $\bar{T}_y^j$ can then be calculated for this sensor:

$$\bar{T}_y^j = \frac{\int_0^{hc} T(y)\, j(y)\, dy}{\int_0^{hc} j(y)\, dy} = 0.464 T(x) \tag{10}$$

Based on this result, we can estimate that impedimetric temperature measurement of any control volume would return 46.4% of the substrate temperature. This estimate is subject to some variation, because the current and temperature functions

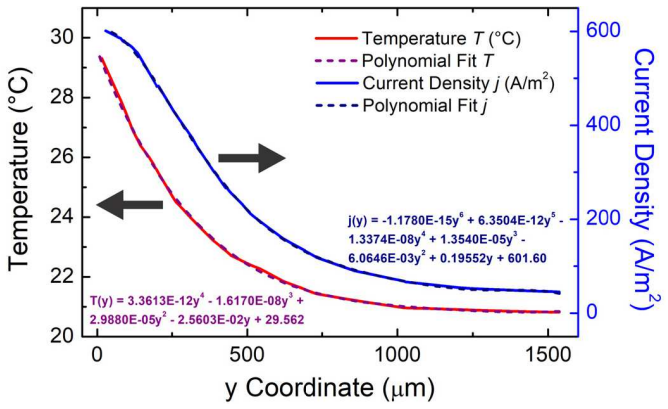


Fig. 5. FEA was used to model the distribution of temperature and current density in the fluid above the sensor. Data are sampled from a line midway between and aligned with each sensing electrode in $x$ and $z$. Polynomial fits of sufficient degree were applied to each distribution to enable current density weighted temperature compensation (see section III-C).

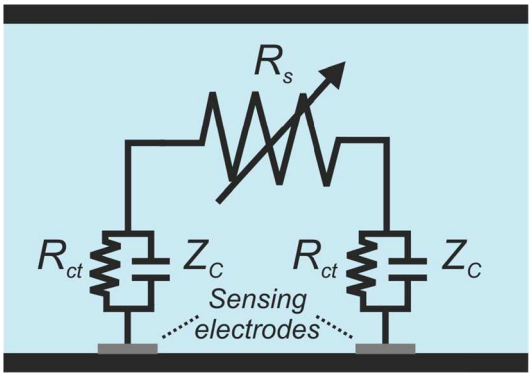


Fig. 6. The simplified Randles' circuit contains a double layer capacitance in parallel with a charge transfer resistance to model the electrode interface, in series with solution resistance.

shown in Fig. 5 depend on axial location and flow velocity. The above estimate was made just downstream of the sensing electrodes ($x = 500$ $\mu$m) at $u = 670$ $\mu$m/s.

As in section III-A, we assumed uniform temperature and current density across $z$. The situation in $x$ is complex due to the semi-infinite boundary conditions we imposed as the electrolyte column extends from both sides of the sensor through lengths of tubing. We defined the upstream and downstream limits of the EAV in $x$ as $l_u$ and $l_d$. An unweighted average of fluid volume between these limits was taken as an approximation of the physical EAV, which would in reality be larger.

To compare the theoretical output to experimental data, the electrode-electrolyte-electrode path was modeled as a simplified Randles' circuit (Fig. 6) [65]. To calculate the solution resistance term $R_S$, the total conductivity $\kappa$, which is the sum of the constituent equivalent conductivities, is required:

$$\kappa = \sum\nolimits_i c_i \left| z_i \right| \Lambda_i \tag{11}$$

where $c_i$ is concentration and $z_i$ is valence of ion $i$. Solution resistance can then be modeled using the following expression for spreading resistance, or the resistance from current spreading infinitely into solution from one electrode, modified from the source to account for two equally-sized rectangular electrodes in series [66]:

$$R_S = \frac{2 \ln 4}{\kappa \pi \sqrt{l_e w_e}} \tag{12}$$

where $l_e$ and $w_e$ are the length and width of the sensing electrode.

The double-layer capacitance forms when counterions assemble near the electrode-electrolyte interface in varying degrees of adhesion. Inquiry into the precise nature of this capacitance and its dependencies is still ongoing [67]–[72], and the effect of temperature in particular remains unclear. From typical experimental values for the platinum/electrolyte interface [70], the estimated magnitude of the apparent capacitance is 60 $\mu$F/cm$^2$, resulting in a reactance $Z_C$ of $\sim$350 $\Omega$ at a typical measurement frequency of 50 kHz. The charge transfer resistance $R_{ct}$ in parallel with $Z_C$ is typically $>$400 k$\Omega$ and can be disregarded [66].

From the above analysis, the expression for the total apparent impedance $Z_a$ of the electrochemical circuit is:

$$Z_a(T) = R_S(T) + 2Z_C \tag{13}$$

The response $Z_a$ is calculated as an average over the EAV. To compare against experimental data, the normalized difference $\Delta \hat{Z}_a$ between $Z_a$ for a given flow rate versus $Z_a$ at ambient temperature $T_{amb}$ can then be calculated:

$$\Delta \hat{Z}_a(T) = 100 \times \frac{Z_a(T) - Z_a(T_{amb})}{Z_a(T_{amb})} \tag{14}$$

## IV. Model Output Analysis

### A. Effects of Sensor Design Choices

Model input parameters were adjusted to predict sensor behavior. Decreasing the thermal conductivity of the channel wall increases sensitivity especially at low flows (Fig. 7a). This is due to the decreased conductive heat loss, which results in more available heat for dissipation through the convective (flow-dependent) mechanism. Some specialized polymers such as fiberglass with known low thermal conductivities may be used as the channel material to increase performance for certain applications.

The trend for EAV size in $x$ suggests that constraining the EAV close to the heater will slightly improve sensitivity and response magnitude, as longer EAV's contain more cold fluid and therefore contribute a weaker thermal signal (Fig. 7b). It is unclear how electrode spacing in $z$ affects EAV, but alternate designs with electrodes arranged parallel to flow can more easily achieve tuning of $l_{u,d}$ (see section VII-E).

Decreasing the channel diameter should flatten the response curve, so that increased linearity and range are traded for higher sensitivity at low flows (Fig. 7c). For applications with flow rates in the hundreds of microliters per minute, shrinking the channel likely confers the most efficient gain in overall performance. Additionally, while the analytical model here cannot predict time-dependent effects, it is anticipated that a smaller fluid volume per length will result in shorter settling times from flow rate changes due to the smaller total thermal mass. Potential downsides of a narrow channel include the

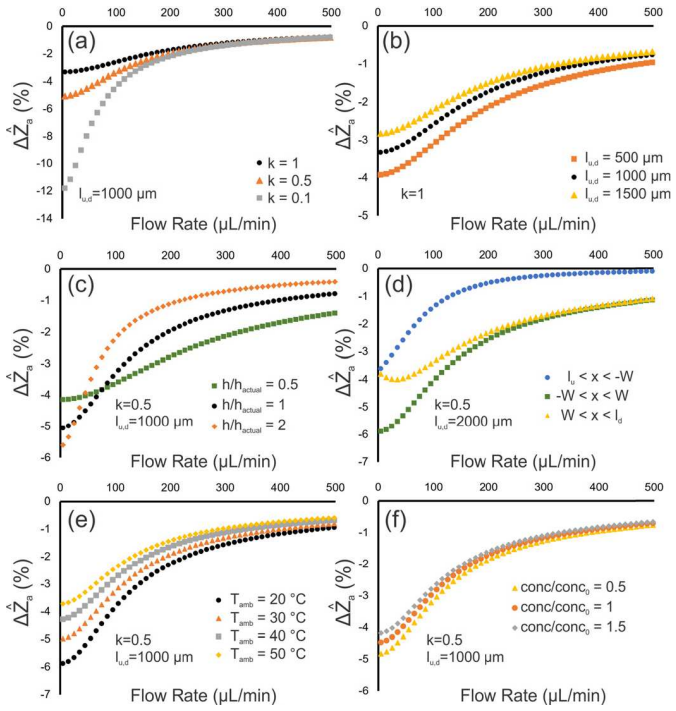


Fig. 7. These plots show the effect of (a) channel wall thermal conductivity, (b) EAV limits in $x$, and (c) channel height on sensor response. (d) Behavior in upstream, downstream, and above-heater fluid subvolumes is also shown. The effects of environmental variables are presented, specifically (e) ambient temperature and (f) concentration. The simulated heater power is 10 mW for all plots.

requisite smaller electrodes and corresponding lower SNR. In addition, there is increased occlusion risk for implanted sensors [73].

Sensor response in subvolumes of the overall EAV was also examined. Distinct behavior was observed in the fluid upstream of, downstream of, and just above the heater (Fig. 7d). Notably, the downstream fluid segment responds negatively to flow up until a certain inflection point, disrupting the overall response curve. In contrast, the upstream and above-heater segments exhibit similar sensitivities. Therefore, shifting the electrode pair upstream should improve both linearity and sensitivity.

### *B. Effects of Environmental Variability*

The effects of environmental change on sensor response are relevant, especially in biological applications where high variability is expected. Lower ambient temperature results in slightly decreasing sensitivity and rather large shifts in the response curve (Fig. 7e), suggesting that compensation is required if temperature variation is expected. This effect is largely attributed to the temperature effect on viscosity [58] and has been validated empirically in related EI thermal flow sensors [74].

In contrast, large changes in ion concentration are well-tolerated by the sensor thanks to normalization of the response to solution conductivity at ambient temperature (Fig. 7f), suggesting consistent performance regardless of varying bodily fluid compositions and patient hydration states. Experimental data for this and other parameters has been gathered for related sensors in prior work [24]; such sensors were not greatly affected by solute concentration change, supporting model results here.

## V. Finite Element Modeling and Results

Numerical simulation was performed in three dimensions using COMSOL Multiphysics (COMSOL Inc., Stockholm, SE). The sensor was modeled as a thin rectangle centered in a fluid channel and the model consisted of 191,010 free tetrahedral mesh elements.

Heat transfer from the heater, a constant power source, and through the fluid and substrate were considered. Fluid velocity was also considered, with the column walls modeled using a no slip boundary condition. Electrical current through the fluid was modeled by assigning the fluid a bulk conductivity and assuming a DC voltage differential between sensing electrodes. Aspects specific to electrochemical current flow such as electrode kinetics and concentration-dependent conductivity effects were neglected for simplicity. Steady state simulations were performed to replicate behavior at equilibrium. Electrodes, heater, and substrate sizes were equal to fabricated device dimensions. The plastic enclosure was modeled as a cylinder of fluid and was extended axially to model silicone tubing connected at its end. The heater and each electrode were modeled as uniform blocks of platinum embedded in the Parylene substrate, omitting the serpentine trace patterning of the heater. Convective cooling of the enclosure with air was assumed. The heat transfer coefficient was calculated according to:

$$h = {}^{k}/_{t} \tag{15}$$

where $k$ is thermal conductivity and $t$ is wall thickness. Because the enclosure material is proprietary and thus $k$ is unknown, $h$ was adjusted to obtain reasonable results. In terms of fluid flow, a fully developed laminar flow profile was assumed to enter the enclosure with average velocity 670 $\mu$m/s. These parameters were used unless otherwise noted.

At steady state, an increase in fluid temperature centered on the heater is apparent (Fig. 8a). Radial temperature slices are also presented (Fig. 8b), in which the slight skew of the temperature distribution downstream expected in calorimetric sensing can be discerned. The color of the thin lines descending from each slice is the temperature of the housing encasing the fluid cylinder.

Fluid velocity was represented using planar heatmaps in the $xy$ (Fig. 9a) and $yz$ (Fig. 9b) planes. The fully-developed input boundary condition is clearly visible in the undisturbed region of pipe to the left of the sensor substrate, with the maximum velocity equal to double the average input velocity, as expected. As the flow is bifurcated by the substrate, the laminar profile is disrupted for a distance $L$ known as the entrance length, which can be estimated according to [75]:

$$L = 0.035ReD = 123\mu\text{m} \tag{16}$$

where $Re$ is the Reynolds number and $D$ is channel diameter. This result supports Fig. 9 and suggests that the flow sensor interacts with fluid primarily in the laminar regime.

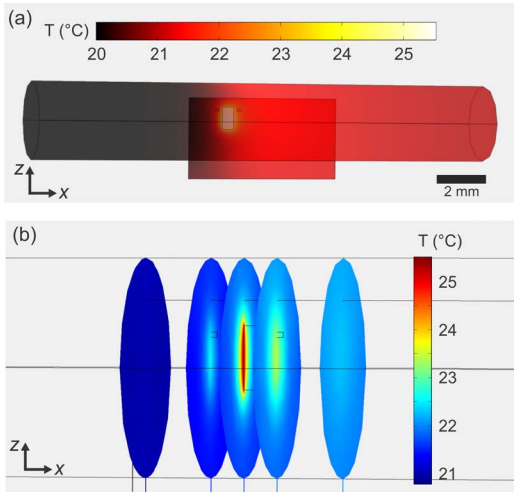


Fig. 8. Thermal response of sensor at 10 mW heater power and 200 $\mu$m/s with flow moving from left to right. (a) Volume heatmap plot of fluid and substrate. (b) The fluid temperature distribution taken at 5 $yz$ planes. Inner planes are centered on the heater and sensing electrodes, while outer planes are $\pm$1500 $\mu$m from the heater.

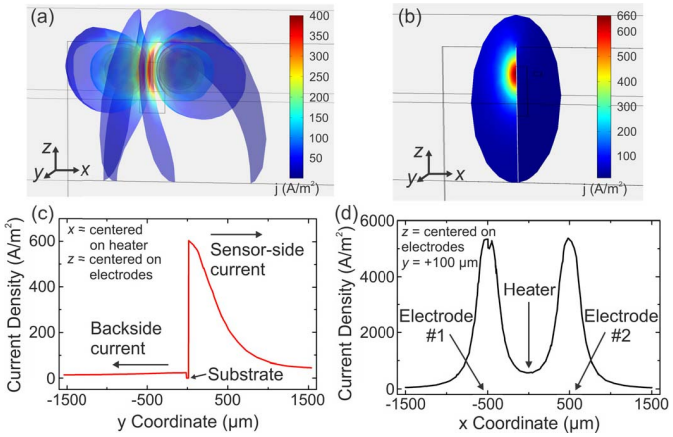


Fig. 10. a) Volume voltage isosurface plot of fluid near the sensing electrodes. Coloring indicates current density. b) $yz$ plane slice of current density, centered equidistantly between sensing electrodes. c) Current density along a $y$ data line located in the same plane as in (b) in $x$, centered with the sensing electrodes in $z$. d) Current density along the $x$-direction centered on the sensing electrodes in $z$, and 100 $\mu$m above the substrate in $y$.

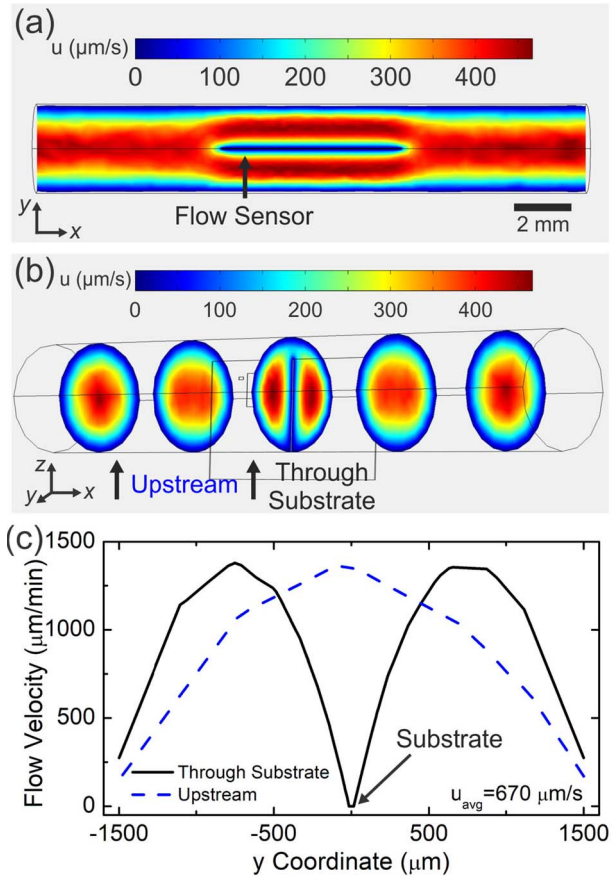


Fig. 9. (a) The $xy$ plane fluid velocity (u) distribution around the sensor film. Arrow indicates flow sensor. (b) The fluid velocity magnitude taken at 5 $yz$ planes. (c) Flow velocity along $y$-direction centered in the sensor enclosure in $z$ ($x$ locations indicated in (b)).

The arrow in Fig. 9a indicates the sensor, which is 700 $\mu$m downstream from the substrate edge. Model results confirm this analytical result, with fully developed flow at the sensor location (Fig. 9c).

Mapping current density facilitates identification of fluid contributing to sensor response. A 3D isovoltage surface plot was generated (that is, each surface is a locus of all points at some voltage). The coloration of each surface indicates current density (Fig. 10a). For this plot, 100 equally spaced potentials are shown. Most of the current passes through fluid just above the front side of the substrate, centered on the sensing electrodes in $z$, as seen in the $yz$ slice of current density (Fig. 10b). Current density along the $y$-direction passing orthogonally through the substrate plane is also presented (Fig. 10c), showing some current passing behind the substrate as well. Current density along the $x$-direction 100 $\mu$m above the sensing electrodes reveals peaks above each electrode which decay to 1% of their maximum after ~1 mm (Fig. 10d).

These results suggest that regions of high current density will be overly represented when transducing temperature. As in (10), the current density-weighted temperature average $\bar{T}^j$ throughout the fluid volume was calculated according to the following formula, this time using volume integration over the entire fluid:

$$\bar{T}^j = \frac{\iiint_{fluid} T j dx dy dz}{\iiint_{fluid} j dx dy dz} \tag{17}$$

where $T$ and $j$ are the temperature and current density function in $x$, $y$, and $z$. This method naturally accounts for the changing position and width of sampled fluid and varying current density within that fluid, allowing comparison with experimental data.

## VI. Experimental Methods

The resistive heater was controlled using 3.3 V square wave pulses (2400 SourceMeter, Keithley Instruments, Solon, OH) and impedance was measured at 50 kHz, as sensor resolution and sensitivity were found empirically to not improve past ~35 kHz (4980A Precision LCR Meter, Keysight Technologies, Santa Clara, CA); experiments and

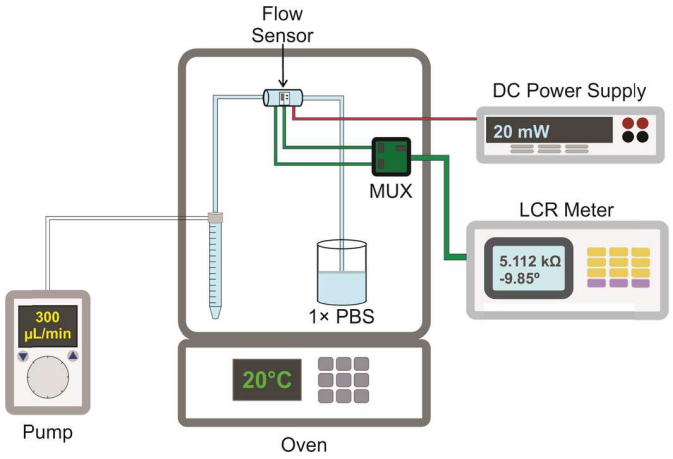


Fig. 11. Typical experimental configuration for flow sensing. The test fluid and sensors are kept within the sealed oven for precise temperature control.

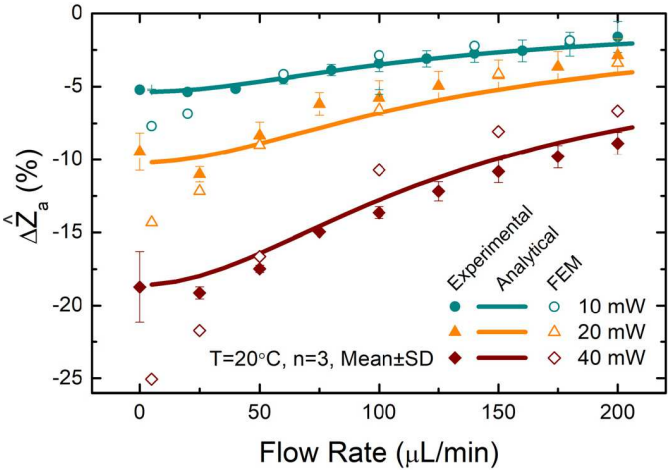


Fig. 12. Simulation fitting to experimental results using $k$ and $l_{u,d}$. Analytical model outputs are solid lines, finite element model outputs are unfilled points, and experimental data are filled points.

data collection were automated via LabView, which acquired data at 5 Hz. The heater was biased at constant power using a PID algorithm, resulting in a overheat temperature of 1.75 – 6.02 °C. Phosphate-buffered saline (PBS) was chosen for testing as a common analog for physiological fluids. Flow was driven with a pressure-controlled, pneumatic, and gravimetrically-calibrated pump for precise flow control (Flow EZ, Fluigent, Paris, FR). A multiplexer array consisting of four ADG1206 ICs (Analog Devices, Norwood, MA) enabled alternating measurements between electrode pairs at 5 Hz. The sensor and fluid under test were housed in a temperature enclosure (EC0A, Sun Electronic Systems, Titusville, FL) to control ambient temperature (Fig. 11).

Impedances of the active and reference cells were normalized to their respective initial values to account for slight differences in electrode impedance which arise during fabrication and packaging. These normalized impedances were then subtracted during heater activation to attenuate conductivity drift.

## VII. Experimental Results

### A. Input Power and Model Validation

Analytical and finite element model results were fitted to experimental data at three different input powers (Fig. 12). For the analytical model, fitting using the model parameters $k$ from (3) and with $l_u = l_d$, the upstream and downstream limits in $x$ of the EAV, yielded $k = 0.5$ and $l_{u,d} = 1900$ $\mu$m. These fits are physically reasonable (the thermal conductivity of plastic is similar to the proprietary channel wall material range from 200 to 500 mW/(m K) compared with water at 598 mW/(m K), for instance) and demonstrate the validity and predictive power of the model. The high variance in experimental data at stagnant flow is due in part to the long settling time characteristic of low flows, which can obscure the steady state point and increase error. The characteristic inflection point at low flows observable in both analytical and experimental data is encouraging and suggests good model accuracy. Sensitivity, resolution, and linearity were calculated for each input power from 20/25 - 200 $\mu$L/min (Table I). Sensitivity is the slope of the linear fit between sensor response in absolute impedance drop versus flow rate. Resolution was calculated by dividing sensitivity by the twice the average standard deviation per point ($2\sigma$ resolution). The coefficient of determination ($R^2$) versus the linear fit was used to quantify linearity.

TABLE I
Experimental Sensor Performance at 3 Input Powers

| Input Power (mW) | Overheat Temp. (°C)[a] | Sensitivity (Ω µL$^{-1}$ min) | Resolution (µL min$^{-1}$)[b] | $R^2$ |
|---|---|---|---|---|
| 10 | 2.89 | 1.23 | 51.9 | 0.978 |
| 20 | 6.17 | 2.91 | 45.6 | 0.907 |
| 40 | 15.15 | 4.38 | 17.4 | 0.975 |

[a]Transduced using heater as RTD. [b]2σ resolution.

FEM-derived results fell within experimental standard deviation for most points at 10 and 20 mW. Divergence at low flows was ascribed to the long times necessary to reach steady state, which may have resulted in premature recording of data. Model predictions at 40 mW were 3 – 5 °C colder than experimental data, which likely resulted from not including a sufficiently long fluid column in the model, such that the far downstream temperature effects which occur at higher velocities and heater temperatures were not included and requires further evaluation.

### B. Impedance Drift in Adjacent Cells

Sensor design assumed that adjacent measurement cells record congruent impedance drift signals. We tested this assumption by interrogating two adjacent cells with no heater activation at zero flow, allowing each signal to freely drift (Fig. 13a). After several minutes of settling time, the differential signal was quite constant, varying only ~50 Ω nonmonotonically over 45 minutes.

A similar experiment was performed using an active heater and a fluid flow. The response of both the active and reference cell were unstable due to downward drift with time (Fig. 13b). The four input flow rates and their timing are indicated

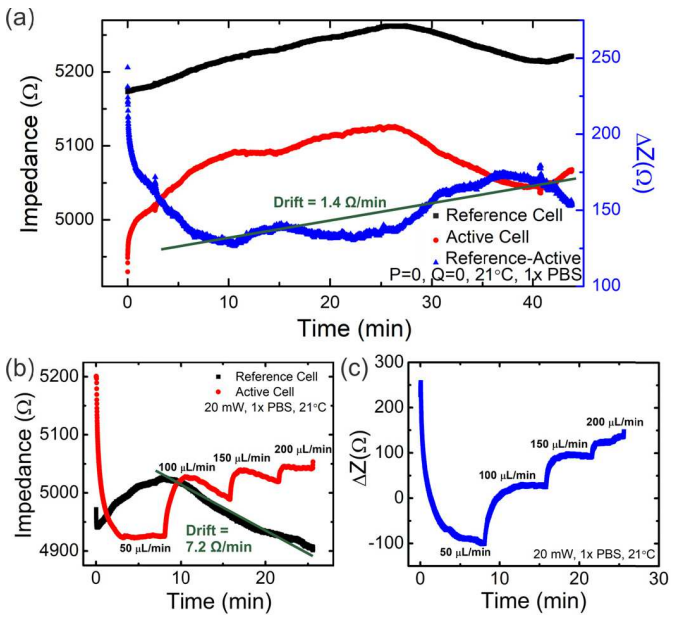


Fig. 13. (a) Impedance drift in adjacent cells with no heater activation or flow. (b) Drift with heater activation at four set flow rates. (c) Differential signal from (b).

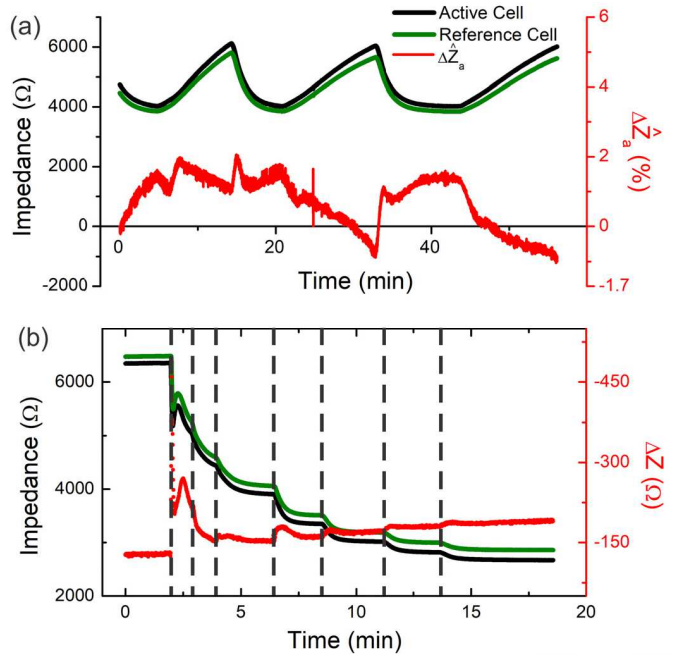


Fig. 14. Results of (a) temperature cycling and (b) PBS concentration increase on the impedances of adjacent cells. The differential signal corresponding to the right ordinate axis is also shown. Dotted lines indicate PBS aliquot addition.

on the graph. By measuring the differential impedance signal, flow rate can be transduced in this proof-of-concept demonstration (Fig. 13c).

Drift resistance was also tested under more disruptive conditions. In one experiment, the ambient temperature of adjacent cells was rapidly cycled using the temperature enclosure set to 60 °C and an ice pack originally at −4 °C (Fig. 14a). In this way, the common-mode impedance was cycled between 4-6 kΩ (∼20–40 °C). Again, the difference

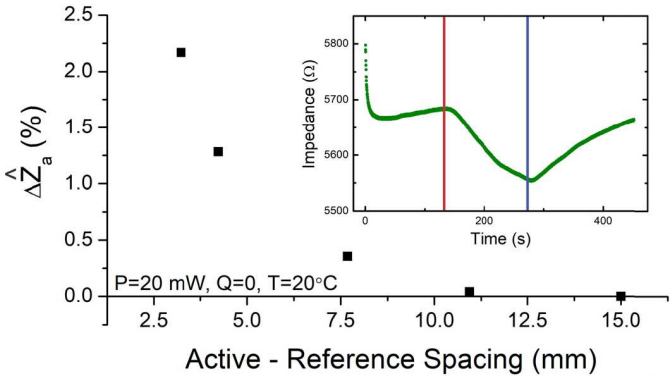


Fig. 15. The maximum impedance response at various separation distances between the active and reference cells is shown. Inset: representative plot of an impedance trace in the reference cell. Red and blue bars indicate heater activation and deactivation, respectively.

signal showed only minor nonmonotonic drift over ±2% of the original impedance offset over 56 minutes, indicating acceptable drift-compensation performance beyond a physiological range.

Solution conductivity was also adjusted by adding 6 sequential 500 $\mu$L aliquots of 10× PBS to a beaker containing 10 mL of 1× PBS and two impedimetric cells (Fig. 14b). The difference in impedance between each cell was constant apart from transients occurring after addition of the PBS concentrate. A drift of 4.20 Ω/min was observed in the differential signal, as opposed to the 270 Ω/min drift in the uncompensated signals.

### C. Reference and Active Cell Spacing

The impedimetric cells must be placed far enough apart to avoid any detection of the active thermal signal in the reference cell. This thermal crosstalk, should it occur, would be detected as an ambient temperature increase and induce error. To determine the minimum acceptable separation distance in the worst case (i.e. at stagnant flow), impedance was measured across 6 electrode pairs placed at set distances from an active heater. The first 2 pairs were fabricated on the same die as the heater, the next 3 were on a die placed adjacently in the same Luer module, and the final pair was on a device in a separate module. The heater was operated for ∼180 s, then the maximum response was recorded (Fig. 15). Results indicate that the sensor should be operated with cells >10 mm apart, where the thermal crosstalk is comparable to other sources of experimental error. Note these impedance changes are due to conductive heat transfer only; at even modest forward flows, forced convective transfer would narrow the acceptable separation distance significantly (see Fig. 1).

### D. Response Time

The time necessary for impedance of the active cell to reach a steady state was measured at 4 different input powers (Fig. 16). Warm-up time was calculated by activating the cold heater, then recording impedance after it was constant for ∼2 minutes. The maximum possible warm-up time was

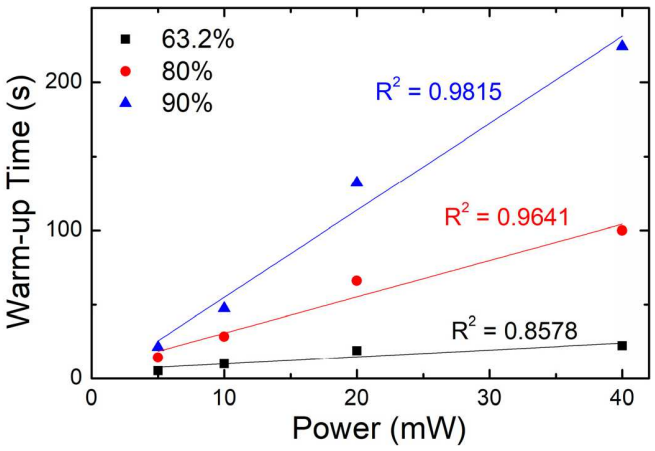


Fig. 16. Sensor warm-up times at four different input powers are plotted. Each data set indicates the necessary time to reach the given percentage of the final impedance value.

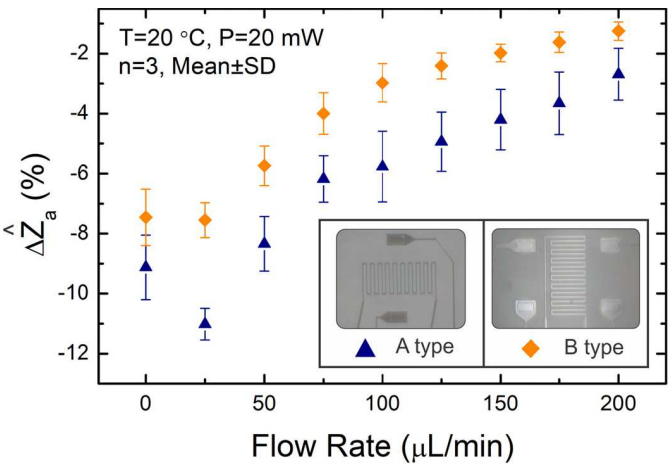


Fig. 17. Experimental sensor response curves from two device variants. In type B, impedance is measured between the top two electrodes as pictured. Data suggests device type B has a wider EAV than A.

obtained by measuring at stagnant flow. Results indicate a linear relationship between input power and warm-up time. The time necessary for impedance to reach a certain percentage of its final value (indicated in the legend) describes varying levels of performance.

The actual response time varies with flow velocity due to differing rates of convective heat loss [76]. Since the actual flow rate is not known *a priori*, the maximum response time should be the reported value. The warm-up time represents the largest possible temperature change during normal operation and is therefore equal to the response time. Assuming a target of 63.2% of the final value, sensor response time at 20 mW is 18.9 seconds.

### *E. Varying Design Geometry*

Two device variants were tested experimentally, one with electrodes above and below the heater (type A) and one with electrodes upstream and downstream of the heater (type B). The heat distribution through the channel should be similar for both device variants, because the channel geometry is unchanged. However, it is expected that the EAV would vary in shape and size between variants. The experimental data shows a decreased magnitude of response from type B compared to type A, which appears mostly independent of flow rate (Fig. 17). This dampened response suggests type B devices have a wider EAV (higher values of $l_{u,d}$) due to the lower average temperature (see Fig. 7b).

### *F. Hysteresis*

The degree of hysteresis was characterized by increasing, then decreasing flow rate through the sensor throughout its range. There was negligible hysteresis in the sensor through 3 full testing cycles (Fig. 18a). One cycle of raw data used to construct the calibration curve is shown (Fig. 18b).

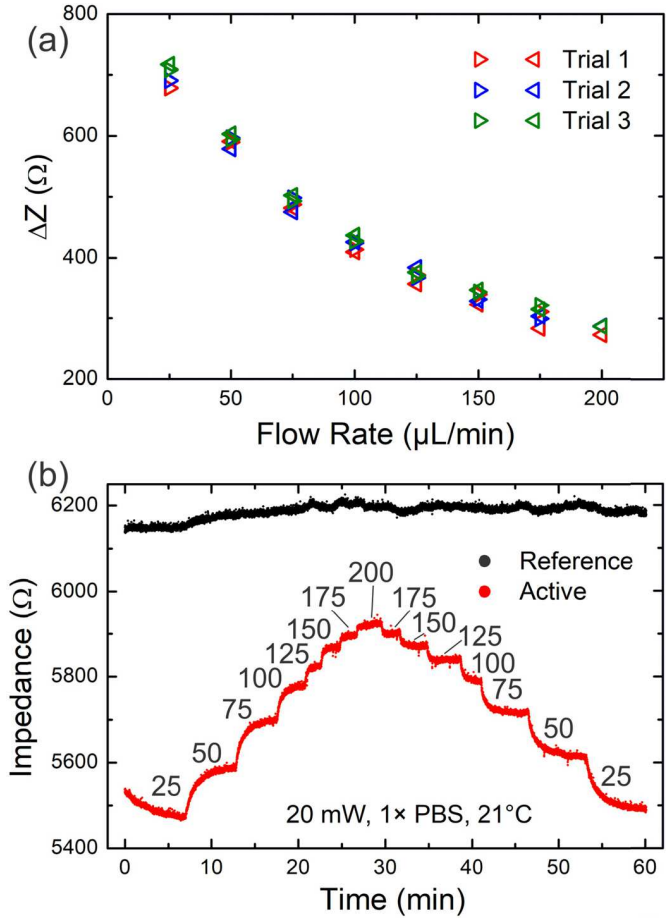


Fig. 18. (a) Sensor hysteresis is plotted over three consecutive trials. Each trial is seven data points with increasing flow rates (right-facing triangles) followed by seven with decreasing flow rates (left-facing triangles). (b) Raw reference and active cell hysteresis data from one trial. Flow rates are in $\mu$L/min.

## VIII. Discussion

EI-based thermal flow sensing can provide highly sensitive flow measurements in a small form factor and at low overheat temperatures. Such sensors are conducive to lightweight wireless interrogation [77] and could thereby enable the collection of personalized, granular biomedical data through distributed implantable sensing networks. More complete characterization of these sensors accompanied by modeling establishes their strengths and limitations and can provide a roadmap for further development.

TABLE II
MICROFABRICATED EI AND THERMAL FLOW SENSORS REPORTED IN LITERATURE AND INDUSTRY

| | Substrate Material | Transduction Method | Sensitivity | Linear Range (µL/min) | Overheat T (°C) | Minimum Detectable Value | Resolution (µL/min) | Response time (s) |
|---|---|---|---|---|---|---|---|---|
| Vilares 2010 [78] | SU-8 | RTD-based calorimetry | 485 µV/(µL/min) | ±2 | 50 | NR | 0.04 | NR |
| Dijkstra 2008 [79] | SiN | RTD-based calorimetry | 218 µV/(µL/min) | 0–0.3 | 34 | 40 nl/min | 0.2 | NR |
| Hoera 2016 [12] | Glass/ PDMS | Video processing of thermally sensitive polymer | 0.78 K/(µL/min) | ±500 | ~40 | 10 nL/min | NR | NR |
| LD20 2020 [80] | Glass | Thermal | NR | 0-16,666 | NR | 41.7 µL/min | 41.7 - 833 | 0.12 |
| Ayliffe 2003 [26] | Glass | EI | NR | 0-4.8 | - | 2.4 µL/min | 2.4 | NR |
| Baldwin 2016 [24] | Parylene | Thermal EI (time of flight) | NR | ±400 | 1 | 43.3 µL/min | 43.3 | ~15* |
| This Work† | Parylene | Thermal EI (anemometry) | 22.3 µV/(µL/min) | 43.0-200 | 6.17 | 43.0 µL/min | 45.6 | 18.9 |

NR = not reported. *Does not include required sensor cooldown time of 1 minute, yielding one measurement per ~75 s. †Values at 20 mW.

By measuring the temperature of fluid directly above the heater, we realized an impedimetric analog of a traditional hot-film anemometer, which instead measures the temperature of the active heating element. The sensitivity and resolution of this device are comparable to previously-reported EI flow sensors [24], [30], but can be measured continuously, obviating the need for cooldown time. Additionally, previous pulsed designs required precise timing and clean data recording for accuracy. This measurement scheme is much more tolerant of the low-power, noisy implantable environment, as a series of measurements can be quickly collected and averaged if necessary.

Sensor performance is compared with other thermal flow sensors in Table II. Experimental sensitivity values in $\Omega\ \mu L^{-1}$ min can be converted to $\mu V\ \mu L^{-1}$ min for comparison with existing flow sensors in the literature assuming a low-side current sensing circuit [81]. Assuming a 2V source and 100 Ω shunt resistor, the sensitivity at 20 mW would be 22.3 $\mu V\ \mu L^{-1}$ min over 43 – 200 $\mu L\ min^{-1}$, which compares favorably to existing rigid substrate-based sensors of similar ranges. Vilares *et al.* [78] and Dijkstra *et al.* [79] report roughly one order of magnitude higher sensitivities (485 and 218 $\mu V\ \mu L^{-1}$ min), but at two orders of magnitude lower ranges (0 – 6 and 0 – 2 $\mu L\ min^{-1}$). Overheat temperatures used in this work (6.17 °C) are also much lower than were reported (50 and 34 °C, respectively). Response times for this work are similar to relevant impedimetric sensors but are much higher than reported for conventional devices, which are typically in the tens of milliseconds to low seconds range. EI sensor response time performance will likely lag that of RTD and thermocouple-based thermal sensors due to the thermal inertia of the large sensitive fluid volume, but a clear roadmap for additional improvement exists due to model results presented here (see discussion below). The minimum detectable flow rate for this work was calculated by subtracting twice the average standard deviation from the response of the B type device at zero flow (Fig. 17), then finding the corresponding flow rate value. The result of 43 $\mu$L/min is again similar to existing EI sensors but falls short of traditional substrates. Moving sensing electrodes to increase linearity in future designs would greatly improve performance here. Similarly, resolution is limited by imperfections in fabrication, packaging, and age differences between measurement cells inherent to academic device prototypes, leading to varying rates of drift and flow response. The development of more automated, jig-based construction of such devices could improve sensor performance.

The current design is restricted to unidirectional flows, since the reference cell must be placed upstream of the active cell. However, a second reference cell could be included to enable bidirectional flow sensing.

Sensor drift in liquid systems is often problematic. The same mechanism which confers high sensitivity for EI sensors – interrogating fluid temperature directly, with no passivation layer – contributes additional drift, because EI is a function of other quantities such as ionic concentration and identity, pressure [57], and electrode impedance and size [82], [83]. The EI reference cell shows promise in mitigating these effects on flow transduction accuracy. Drift can also occur from ingress of solution across the Parylene film, which can be particularly impactful for multi-layer polymer devices [84]. Referenced measurements are expected to eventually fail due to stochastic deviations in solution ingress between cells but appear successful over the time scales tested.

Modeling results provided actionable results for future designs to improve sensor range, linearity, and sensitivity. Over the parameters swept, future sensors should minimize the thermal conductivity of the channel material, minimize inter- electrode spacing, and minimize channel diameter. Sensing electrodes could also be placed upstream of the heater to improve linearity at low flows. These changes should improve the senstivity, linear range, and response time of the sensor.

A weakness of the current approach is its response time performance at no flow. Response times at stagnant flows are high but shorten significantly with increasing velocity, typically approaching 1/3 of the no flow response time [76], [85] There is a tradeoff between sensitivity or resolution and response time when adjusting input power which can be tailored to the application. Strategies to improve response time are known and include changes to fabrication, packaging, and sensing algorithm [86]. Long response times may be acceptable in chronic implantable applications involving low-frequency, slow flows [87].

The sensitivity minimum at very low flows (see Fig. 12) also disrupts response linearity. This behavior was known to be possible after modeling given the crossover in downstream temperature with increasing flow rate in Fig. 4. However, EAV size was unknown and thus the degree of nonlinearity of fluid about the heater could not be anticipated. Moving the sensing electrodes upstream of the heater in future designs should notably improve performance by sampling a different and more linear fluid subvolume (see section IV-A).

The real-world application of implantable flow sensing involves confounding factors not explored in this work, e.g. mechanical flexion, noise from vibration and micro-motion, and pulsatility. For soft polymer devices packaged without a hard thermoplastic channel, bending and torsion in particular would be expected to change the EI response due to varying interelectrode spacing. Preliminary results with mechanical shaking and flow rate pulsatility using pulsed heater activations showed little effect on sensor response (data not shown). A similar or lesser effect is expected using continuous sensing, considering the low response bandwidth of the sensor, but further work is necessary to confirm this. Future work will also explore sensor behavior *in vivo* as in the drainage of CSF in porcine models [88].

## IX. Conclusion

An impedimetric analog of a traditional hot-film sensor was presented. Long-term sensing was enabled via an identical companion cell to attenuate common-mode EI drift. Continuous sensing significantly improved response times compared with prior EI sensors. Analytical and finite element models for EI-based thermal flow sensing showed good agreement with experimental data and provided avenues for future development. Best practices for input power and cell spacing were discussed, and response time as well as an alternate sensor layout were characterized. The sensor is ideal for biological fluid tracking and implantable applications due to its biocompatible construction, low power, low overheat temperatures, and noise tolerance compared with previous EI sensors.

## Appendix

Expressions from MSA theory for the dielectric and electrophoretic correction factors to the limiting conductivity are below [62], [63]. The dielectric correction factor is composed of three factors:

$$\frac{\delta X}{X} = \frac{\delta X_1^{rel}}{X} + \frac{\delta X_2^{rel}}{X} + \frac{\delta X^{hyd}}{X}$$

where $\frac{\delta X_1^{rel}}{X}$ and $\frac{\delta X_2^{rel}}{X}$ are first and second order contributions and $\frac{\delta X^{hyd}}{X}$ is due to hydrodynamic interaction.

The first order contribution is as follows:

$$\frac{\delta X_1^{rel}}{X} = -\frac{\kappa_q^2}{3}\left[i_0 - \frac{\epsilon k_B T}{e_i e_j}\kappa_q \sigma_{ij}^2 i_1\right] \times \frac{-\kappa_q A_{ij}\exp\left(-\kappa_q \sigma_{ij}\right)}{\kappa_q^2 + 2\Gamma\kappa_q + 2\Gamma^2 - \left(2\Gamma^2/\alpha^2\right)\sum_k \varrho_k a_k^2 \exp\left(-\kappa_q \sigma_k\right)}$$

where

$$i_0 = \frac{\sinh\left(\kappa_q \sigma_{ij}\right)}{\kappa_q \sigma_{ij}}$$

$$i_1 = \frac{\cosh\left(\kappa_q \sigma_{ij}\right)}{\kappa_q \sigma_{ij}} - \frac{\sinh\left(\kappa_q \sigma_{ij}\right)}{\kappa_q^2 \sigma_{ij}^2}$$

$$\kappa_q^2 = \frac{4\pi}{\epsilon k_B T}\frac{\varrho_i e_i^2 D_i^0 + \varrho_j e_j^2 D_j^0}{D_i^0 + D_j^0}$$

Here, $\varrho_i$ is the number density of ion $i$, $\sigma_i$ is the crystallographic diameter of ion $i$, $e_i = z_i e$ is the charge of ion $i$ where $z_i$ is the valence and $e$ is the elementary charge, and the closest approach distance between ions $i$ and $j$ is:

$$\sigma_{ij} = \frac{\sigma_i + \sigma_j}{2}$$

The permittivity of pure solvent converted from *cgs* units is:

$$\epsilon = 4\pi\epsilon_0\epsilon_s$$

where $\epsilon_0$ and $\epsilon_s$ are the vacuum and relative permittivity, respectively. For the diffusion coefficient of ion $i$ at infinite dilution, we use the semiempirical revised Stokes-Einstein relation [89]:

$$D_i^0 = \frac{e^c T}{\eta^d}$$

where $c$ and $d$ are experimental constants. For sodium, $c = 20.2$ and $d = 1$ and for chloride, $c = 19.4$ and $d = 0.95$. Additionally,

$$A_{ij} = \frac{e_i e_j}{\epsilon k_B T\left(1 + \Gamma\sigma_i\right)\left(1 + \Gamma\sigma_j\right)}$$

$$a_k = \frac{\alpha^2}{2\Gamma}\frac{z_k}{1 + \Gamma\sigma_j}$$

$$\alpha^2 = \frac{4\pi e^2}{\epsilon k_B T}$$

The inverse Debye length $\Gamma$ is defined recursively as:

$$4\Gamma^2 = \frac{4\pi e^2}{\epsilon k_B T}\sum_i \varrho_i\left(\frac{z_i - \pi/2\Delta P_n \sigma_i^2}{1 + \Gamma\sigma_i}\right)^2$$

where

$$P_n = \frac{1}{\Omega}\sum_k \frac{\varrho_k \sigma_k z_k}{1+\Gamma\sigma_k}$$
$$\Omega = 1 + \frac{\pi}{2\Delta}\sum_k \frac{\varrho_k \sigma_k^3}{1+\Gamma\sigma_k}$$
$$\Delta = 1 - \frac{\pi}{6}\sum_k \varrho_k \sigma_k^3$$

The magnitude of the second order contribution is ~10% of the first order in our application, and is given by:

$$\begin{aligned}
&\frac{\delta X_2^{rel}}{X} \\
&= -\frac{\kappa_q}{3}\left[i_0 - \frac{\epsilon k_B T}{e_i e_j}\kappa_q \sigma_{ij}^2 i_1\right] \\
&\quad \times A_{ij}^2 \left\{\left(\frac{x^2+\kappa_q^2}{x^2-\kappa_q^2}\right)\left[\frac{\kappa_q^2}{4x^2}\exp\left(2x\sigma_{ij}\right) E_1\left[\left(2x+\kappa_q\right)\sigma_{ij}\right]\right.\right. \\
&\quad + \left.\frac{\exp\left(-\kappa_q\sigma_{ij}\right)}{4x^2\sigma_{ij}^2}\left[1+\left(2x-\kappa_q\right)\sigma_{ij}\right]\right] \\
&\quad + \frac{\kappa_q C_{ij}}{x-\kappa_q}\left[\frac{x^2-2\kappa_q^2}{2\kappa_q\left(x+\kappa_q\right)} \times \exp\left(x\sigma_{ij}\right) E_1\left[\left(x+2\kappa_q\right)\sigma_{ij}\right]\right. \\
&\quad - \left.\frac{\exp\left(-2\kappa_q\sigma_{ij}\right)}{2\kappa_q\left(x+\kappa_q\right)\sigma_{ij}^2}\left(1+x\sigma_{ij}\right)\right] \\
&\quad + \left(1+x\sigma_{ij}\right)\left[\frac{\left(x^2-\kappa_q^2\right)^2}{4x^2\kappa_q^2}\exp\left(x\sigma_{ij}\right) E_1\left[\left(x+\kappa_q\right)\sigma_{ij}\right]\right. \\
&\quad - \frac{x^2}{4\kappa_q^2}\exp\left(\left(x-\kappa_q\right)\sigma_{ij}\right) E_1\left(x\sigma_{ij}\right)\left(1+\kappa_q\sigma_{ij}\right) \\
&\quad + \left.\left.\frac{\exp\left(-\kappa_q\sigma_{ij}\right)}{4x^2\sigma_{ij}^2}\left(1+\left(x-\kappa_q\right)\sigma_{ij}+\frac{x^3\sigma_{ij}^2}{\kappa_q}\right)\right]\right\}
\end{aligned}$$

where

$$\begin{aligned}
C_{ij} &= \cosh\left(\kappa_q\sigma_{ij}\right) + \frac{x}{\kappa_q}\sinh\left(\kappa_q\sigma_{ij}\right) \\
E_1\left(\kappa_q r\right) &= \int_r^\infty \frac{\exp\left(-\kappa_q r\right)}{r} dr \\
x &= 2\Gamma\left(1+\Gamma\bar{\sigma}\right) \\
\bar{\sigma} &= \frac{1}{\alpha^2}\sum_k \varrho_k a_k^2 \sigma_k
\end{aligned}$$

The hydrodynamic contribution is:

$$\begin{aligned}
&\frac{\delta X^{hyd}}{X} \\
&= \frac{-4\Gamma^2 A_{ij} k_B T}{48\pi\eta\left(D_i^0 + D_j^0\right)}\left[i_0 - \frac{\epsilon k_B T}{e_i e_j}\kappa_q\sigma_{ij}^2 i_1\right] \\
&\quad \times \left\{\left(1+x\sigma_{ij}+\frac{x^2\sigma_{ij}^2}{3}\right)\left[\frac{x^2}{\kappa_q^2}\left(\exp\left(\left(x-\kappa_q\right)\sigma_{ij}\right)\right)\right.\right. \\
&\quad \times E_1\left(x\sigma_{ij}\right)\left(1+\kappa_q\sigma_{ij}\right) - \frac{x^2\exp\left(-\kappa_q\sigma_{ij}\right)}{\kappa_q\left(x+\kappa_q\right)} \\
&\quad - \frac{x^2}{\kappa_q^2}E_1\left[\left(x+\kappa_q\right)\sigma_{ij}\right] \\
&\quad + \frac{2x^2-\kappa_q^2}{x^2}\exp\left(x\sigma_{ij}\right) E_1\left[\left(x+\kappa_q\right)\sigma_{ij}\right] \\
&\quad - \left.\frac{\exp\left(-\kappa_q\sigma_{ij}\right)}{x^2\sigma_{ij}^2}\left(1+\left(x-\kappa_q\right)\sigma_{ij}\right) - \frac{x\exp\left(-\kappa_q\sigma_{ij}\right)}{x+\kappa_q}\right] \\
&\quad + \frac{\exp\left(-\kappa_q\sigma_{ij}\right)}{x^2\sigma_{ij}^2}\left(1+\left(2x-\kappa_q\right)\sigma_{ij}\right) \\
&\quad - \left.\frac{4\pi^2-\kappa_q^2}{x^2}\exp\left(2x\sigma_{ij}\right) E_1\left[\left(2x+\kappa_q\right)\sigma_{ij}\right]\right\}
\end{aligned}$$

Next, the electrophoretic correction factor is composed of two factors:

$$\frac{\delta v_i^{el}}{v_i^0} = \frac{\delta v_{i1}^{el}}{v_i^0} + \frac{\delta v_{i2}^{el}}{v_i^0}$$

The first-order electrophoretic correction is:

$$\delta v_{i1}^{el} = -\frac{e_i E}{3\pi\eta}\left(\frac{\Gamma}{1+\Gamma\sigma_i} + \frac{\pi}{2\Delta}\frac{P_n\sigma_i}{z_i\left(1+\Gamma\sigma_i\right)} + \frac{\pi}{z_i}\sum_j \varrho_j z_j \sigma_{ij}^2\right)$$

The second order electrophoretic term is

$$\delta v_{i2}^{el} = I + J$$

where

$$\begin{aligned}
I &= \frac{e_i E\kappa_q^2 A_{ij}}{24\pi\eta\left(x^2-\kappa_q^2\right)\sigma_{ij}^2\left(1+\Gamma\sigma_i\right)\left(1+\Gamma\sigma_j\right)} \\
&\quad \times \left\{\left(1+2x\sigma_{ij}\right) - C_{ij}\exp\left(-\kappa_q\sigma_{ij}\right)\left(1+\left(x-\kappa_q\right)\sigma_{ij}\right)\right. \\
&\quad - 2x^2\sigma_{ij}^2\exp\left(2x\sigma_{ij}\right) E_1\left(2x\sigma_{ij}\right) \\
&\quad + \left. C_{ij}\left(x^2+\kappa_q^2\right)\sigma_{ij}^2\exp\left(x\sigma_{ij}\right) E_1\left[\left(x+\kappa_q\right)\sigma_{ij}\right]\right\} \\
J &= \frac{e_i E}{12\pi\eta\left(1+\Gamma\sigma_i\right)\left(1+\Gamma\sigma_j\right)}\left(\cosh\left(\kappa_q\sigma_{ij}\right) - \frac{\sinh\left(\kappa_q\sigma_{ij}\right)}{\kappa_q\sigma_{ij}}\right) \\
&\quad \times \frac{\kappa_q^3\exp\left(-\kappa_q\sigma_{ij}\right)}{\kappa_q^2 + 2\Gamma\kappa_q + 2\Gamma^2 - 2\Gamma^2/\alpha^2\sum_k \varrho_k a_k^2\exp\left(\kappa_q\sigma_{ij}\right)}
\end{aligned}$$

The velocity of ion $i$ at infinite dilution in voltage field $E$ is:

$$v_i^0 = e_i E\frac{D_i^0}{k_B T}$$

## ACKNOWLEDGMENT

The authors would like to thank Dr. Alex Baldwin for his advice and encouragement, Priya Lee for her experimental assistance, Dr. Donghai Zhu of the USC Core Nanofabrication Facilities for his fabrication assistance, and the members of the Biomedical Microsystems Lab for their helpful discussion.

## REFERENCES


[1] J. T. W. Kuo, L. Yu, and E. Meng, "Micromachined thermal flow sensors—A review," *Micromachines*, vol. 3, no. 3, pp. 550–573, Jul. 2012.

[2] N. T. Nguyen, "Micromachined flow sensors—A review," *Flow Meas. Instrum.*, vol. 8, no. 1, pp. 7–16, Mar. 1997.

[3] F. Ejeian *et al.*, "Design and applications of MEMS flow sensors: A review," *Sens. Actuators A, Phys.*, vol. 295, pp. 483–502, Aug. 2019.

[4] A. E. Kennelly, C. A. Wright, and J. S. Van Bylevelt, "The convection of heat from small copper wires," *Proc. Amer. Inst. Electr. Eng.*, vol. 28, no. 7, pp. 699–729, Jul. 1909.

[5] U. Bordini, "Uii procedimento per la misura della velocita dei gas," *Nuovo Cimento*, vol. 3, pp. 241–283, Oct. 1911.

[6] J. Morris, "The electrical measurement of wind velocity," *Electrician*, vol. 70, p. 278, Nov. 1912.

[7] K. L. Vessot and B. H. Turner, "XII. On the convection of heat from small cylinders in a stream of fluid: Determination of the convection constants of small platinum wires with applications to hot-wire anemometry," *Philos. Trans. Roy. Soc. London A, Containing Papers Math. Phys. Character*, vol. 214, nos. 509–522, pp. 373–432, Jan. 1914.

[8] M. Elwenspoek, "Thermal flow micro sensors," in *Proc. Int. Semiconductor Conf.*, vol. 2, 1999, pp. 423–435.

[9] T. S. J. Lammerink, N. R. Tas, M. Elwenspoek, and J. H. J. Fluitman, "Micro-liquid flow sensor," *Sens. Actuators A, Phys.*, vols. 37–38, pp. 45–50, Jun. 1993.

[10] A. J. van der Wiel, C. Linder, N. F. de Rooij, and A. Bezinge, "A liquid velocity sensor based on the hot-wire principle," *Sens. Actuators A, Phys.*, vols. 37–38, pp. 693–697, Jun. 1993.

[11] V. Balakrishnan, T. Dinh, H.-P. Phan, D. V. Dao, and N.-T. Nguyen, "Highly sensitive 3C-SiC on glass based thermal flow sensor realized using MEMS technology," *Sens. Actuators A, Phys.*, vol. 279, pp. 293–305, Aug. 2018.

[12] C. Hoera *et al.*, "A chip-integrated highly variable thermal flow rate sensor," *Sens. Actuators B, Chem.*, vol. 225, pp. 42–49, Mar. 2016.

[13] F. Shaun *et al.*, "Sensitivity optimization of micro-machined thermoresistive flow-rate sensors on silicon substrates," *J. Micromech. Microeng.*, vol. 28, no. 7, Jul. 2018, Art. no. 074002.

[14] H. Takahashi, A. Nakai, and I. Shimoyama, "Waterproof airflow sensor for seabird bio-logging using a highly sensitive differential pressure sensor and nano-hole array," *Sens. Actuators A, Phys.*, vol. 281, pp. 243–249, Oct. 2018.

[15] V. W. Wong *et al.*, "Mechanical force prolongs acute inflammation *via* T-cell-dependent pathways during scar formation," *FASEB J.*, vol. 25, no. 12, pp. 4498–4510, Dec. 2011.

[16] P. Moshayedi *et al.*, "The relationship between glial cell mechanosensitivity and foreign body reactions in the central nervous system," *Biomaterials*, vol. 35, no. 13, pp. 3919–3925, Apr. 2014.

[17] A. Wang *et al.*, "Stability of and inflammatory response to silicon coated with a fluoroalkyl self-assembled monolayer in the central nervous system," *J. Biomed. Mater. Res. A*, vol. 81A, no. 2, pp. 363–372, May 2007.

[18] J. C. Barrese *et al.*, "Failure mode analysis of silicon-based intracortical microelectrode arrays in non-human primates," *J. Neural Eng.*, vol. 10, no. 6, Nov. 2013, Art. no. 066014.

[19] E. Meng, P.-Y. Li, and Y.-C. Tai, "A biocompatible Parylene thermal flow sensing array," *Sens. Actuators A, Phys.*, vol. 144, no. 1, pp. 18–28, May 2008.

[20] Q. Zhang *et al.*, "Flexible ZnO thin film acoustic wave device for gas flow rate measurement," *J. Micromech. Microeng.*, vol. 30, no. 9, Sep. 2020, Art. no. 095010.

[21] D. Barmpakos, A. Moschos, T. Syrovy, T. Koutsis, L. Syrova, and G. Kaltsas, "A fully printed flexible multidirectional thermal flow sensor," *Flexible Printed Electron.*, vol. 5, no. 3, Aug. 2020, Art. no. 035005.

[22] M. D. Dankoco, G. Y. Tesfay, E. Benevent, and M. Bendahan, "Temperature sensor realized by inkjet printing process on flexible substrate," *Mater. Sci. Eng. B*, vol. 205, pp. 1–5, Mar. 2016.

[23] I.-L. Ngo, S. Jeon, and C. Byon, "Thermal conductivity of transparent and flexible polymers containing fillers: A literature review," *Int. J. Heat Mass Transf.*, vol. 98, pp. 219–226, Jul. 2016.

[24] A. Baldwin, L. Yu, and E. Meng, "An electrochemical impedance-based thermal flow sensor for physiological fluids," *J. Microelectromech. Syst.*, vol. 25, no. 6, pp. 1015–1024, Dec. 2016.

[25] M. W. Dewhirst, B. L. Viglianti, M. Lora-Michiels, M. Hanson, and P. J. Hoopes, "Basic principles of thermal dosimetry and thermal thresholds for tissue damage from hyperthermia," *Int. J. Hyperthermia*, vol. 19, no. 3, pp. 267–294, Jan. 2003.

[26] H. E. Ayliffe and R. D. Rabbitt, "An electric impedance based microelectromechanical system flow sensor for ionic solutions," *Meas. Sci. Technol.*, vol. 14, no. 8, p. 1321, Jul. 2003.

[27] J. Wu and W. Sansen, "Electrochemical time of flight flow sensor," *Sens. Actuators A, Phys.*, vols. 97–98, pp. 68–74, Apr. 2002.

[28] X. Gao and H. S. White, "Rotating microdisk voltammetry," *Anal. Chem.*, vol. 67, no. 22, pp. 4057–4064, Nov. 1995.

[29] A. Baldwin, E. Yoon, T. Hudson, and E. Meng, "Fluid temperature measurement in aqueous solution via electrochemical impedance," *J. Microelectromech. Syst.*, vol. 28, no. 6, pp. 1060–1067, Dec. 2019.

[30] A. Baldwin, T. Hudson, and E. Meng, "A calorimetric flow sensor for ultra-low flow applications using electrochemical impedance," in *Proc. IEEE Micro Electro Mech. Syst. (MEMS)*, Jan. 2018, pp. 361–364.

[31] T. Hudson, A. Baldwin, and E. Meng, "A continuous, drift-compensated impedimetric thermal flow sensor for *in vivo* applications," in *Proc. IEEE 32nd Int. Conf. Micro Electro Mech. Syst. (MEMS)*, Jan. 2019, pp. 731–734.

[32] E. Meng, *Biomedical Microsystems*. Boca Raton, FL, USA: CRC Press, 2011.

[33] B. J. Kim and E. Meng, "Micromachining of Parylene C for bioMEMS," *Polym. Adv. Technol.*, vol. 27, no. 5, pp. 564–576, May 2016.

[34] W. F. Gorham, "A new, general synthetic method for the preparation of linear Poly-*p*-xylylenes," *J. Polym. Sci. A-1, Polym. Chem.*, vol. 4, no. 12, pp. 3027–3039, Dec. 1966.

[35] E. Meng, P.-Y. Li, and Y.-C. Tai, "Plasma removal of Parylene C," *J. Micromech. Microeng.*, vol. 18, no. 4, Apr. 2008, Art. no. 045004.

[36] D. Rodger *et al.*, "Flexible parylene-based multielectrode array technology for high-density neural stimulation and recording," *Sens. Actuators B, Chem.*, vol. 132, no. 2, pp. 449–460, Jun. 2008.

[37] C. A. Gutierrez, C. Lee, B. Kim, and E. Meng, "Epoxy-less packaging methods for electrical contact to parylene-based flat flexible cables," in *Proc. 16th Int. Solid-State Sensors, Actuat. Microsyst. Conf.*, Jun. 2011, pp. 2299–2302.

[38] N. T. Nguyen and W. Dötzel, "Asymmetrical locations of heaters and sensors relative to each other using heater arrays: A novel method for designing multi-range electrocaloric mass-flow sensors," *Sens. Actuators A, Phys.*, vol. 62, nos. 1–3, pp. 506–512, Jul. 1997.

[39] W. Xu, K. Song, S. Ma, B. Gao, Y. Chiu, and Y.-K. Lee, "Theoretical and experimental investigations of thermoresistive micro calorimetric flow sensors fabricated by CMOS MEMS technology," *J. Microelectromech. Syst.*, vol. 25, no. 5, pp. 954–962, Oct. 2016.

[40] W. Xu, S. Ma, X. Wang, Y. Chiu, and Y.-K. Lee, "A CMOS-MEMS thermoresistive micro calorimetric flow sensor with temperature compensation," *J. Microelectromech. Syst.*, vol. 28, no. 5, pp. 841–849, Oct. 2019.

[41] E. Hückel and P. Debye, "The theory of electrolytes: I. Lowering of freezing point and related phenomena," *Phys. Z*, vol. 24, no. 305, pp. 185–206, 1923.

[42] P. Debye and E. Hückel, "Bemerkungen zu einem Satze iiber die Kataphoretische Wanderungsgeschwindigkeit suspendierter Teilchen," *Phys. Z*, vol. 25, no. 49, pp. 49–52, 1924.

[43] L. Onsager, "The theory of electrolytes," *Phys. Z*, vol. 27, no. 388, pp. 388–392, 1926.

[44] L. Onsager and R. M. Fuoss, "Irreversible processes in electrolytes. Diffusion, conductance and viscous flow in arbitrary mixtures of strong electrolytes," *J. Phys. Chem.*, vol. 36, no. 11, pp. 2689–2778, Nov. 1932.

[45] P. Walden, "Über organische Lösungs-und Ionisierungsmittel. III. Teil: Innere Reibung und deren Zusammenhang mit dem Leitvermögen," *Z. Phys. Chem.*, vol. 55, no. 207, pp. 207–249, 1906.

[46] M. Born, "Volumen und Hydratationswärme der ionen," *Zeitschrift für Physik*, vol. 1, no. 1, pp. 45–48, Feb. 1920.

[47] R. M. Fuoss, "Dependence of the Walden product on dielectric constant," *Proc. Nat. Acad. Sci. USA*, vol. 45, no. 6, pp. 807–813, Jun. 1959.

[48] R. H. Boyd, "Extension of Stokes' law for ionic motion to include the effect of dielectric relaxation," *J. Chem. Phys.*, vol. 35, no. 4, pp. 1281–1283, Oct. 1961.

[49] R. Zwanzig, "Dielectric friction on a moving Ion. II. Revised theory," *J. Chem. Phys.*, vol. 52, no. 7, p. 3625, 1970.

[50] J. B. Hubbard, "Dielectric dispersion and dielectric friction in electrolyte solutions. II," *J. Chem. Phys.*, vol. 68, no. 4, pp. 1649–1664, Feb. 1978.

[51] R. Biswas and B. Bagchi, "Limiting ionic conductance of symmetrical, rigid ions in aqueous solutions: Temperature dependence and solvent isotope effects," *J. Amer. Chem. Soc.*, vol. 119, no. 25, pp. 5946–5953, Jun. 1997.

[52] P. G. Wolynes, "Dynamics of electrolyte solutions," *Annu. Rev. Phys. Chem.*, vol. 31, no. 1, pp. 345–376, Oct. 1980.
[53] M. Berkowitz and W. Wan, "The limiting ionic conductivity of $Na^+$ and $Cl^-$ ions in aqueous solutions: Molecular dynamics simulation," *J. Chem. Phys.*, vol. 86, no. 1, pp. 376–382, Jan. 1987.
[54] P. Kumar and S. Yashonath, "Ionic conductivity in aqueous electrolyte solutions: Insights from computer simulations," *J. Mol. Liquids*, vol. 277, pp. 506–515, Mar. 2019.
[55] A. Anderko and M. M. Lencka, "Computation of electrical conductivity of multicomponent aqueous systems in wide concentration and temperature ranges," *Ind. Eng. Chem. Res.*, vol. 36, no. 5, pp. 1932–1943, May 1997.
[56] A. L. Horvath, *Handbook of Aqueous Electrolyte Solutions*. Chichester, U.K.: Ellis Horwood, 1985.
[57] R. A. Robinson and R. H. Stokes, *Electrolyte Solutions*, 2nd ed. Mineola, NY, USA: Dover, 2002.
[58] M. L. Huber *et al.*, "New international formulation for the viscosity of $H_2O$," *J. Phys. Chem. Reference Data*, vol. 38, no. 2, pp. 101–125, Jun. 2009.
[59] J. E. Hall and A. C. Guyton, *Guyton and Hall Textbook of Medical Physiology*, 12th ed. Philadelphia, PA, USA: Saunders/Elsevier, 2011.
[60] D. Irani, "Properties and composition of normal cerebrospinal fluid," in *Cerebrospinal Fluid in Clinical Practice*. Amsterdam, The Netherlands: Elsevier, 2009, pp. 69–89.
[61] G. M. Roger, S. Durand-Vidal, O. Bernard, and P. Turq, "Electrical conductivity of mixed electrolytes: Modeling within the mean spherical approximation," *J. Phys. Chem. B*, vol. 113, no. 25, pp. 8670–8674, Jun. 2009.
[62] O. Bernard, W. Kunz, P. Turq, and L. Blum, "Conductance in electrolyte solutions using the mean spherical approximation," *J. Phys. Chem.*, vol. 96, no. 9, pp. 3833–3840, Apr. 1992.
[63] P. Turq, L. Blum, O. Bernard, and W. Kunz, "Conductance in associated electrolytes using the mean spherical approximation," *J. Phys. Chem.*, vol. 99, no. 2, pp. 822–827, Jan. 1995.
[64] J. L. Lebowitz and J. K. Percus, "Mean spherical model for lattice gases with extended hard cores and continuum fluids," *Phys. Rev.*, vol. 144, no. 1, pp. 251–258, Apr. 1966.
[65] J. E. B. Randles, "Kinetics of rapid electrode reactions," *Discuss. Faraday Soc.*, vol. 1, p. 11, Mar. 1947.
[66] W. Franks, I. Schenker, P. Schmutz, and A. Hierlemann, "Impedance characterization and modeling of electrodes for biomedical applications," *IEEE Trans. Biomed. Eng.*, vol. 52, no. 7, pp. 1295–1302, Jul. 2005.
[67] E. T. McAdams, A. Lackermeier, J. A. McLaughlin, D. Macken, and J. Jossinet, "The linear and non-linear electrical properties of the electrode-electrolyte interface," *Biosensor Bioelectron.*, vol. 10, nos. 1–2, pp. 67–74, Jan. 1995.
[68] J. Huang, T. Zhou, J. Zhang, and M. Eikerling, "Double layer of platinum electrodes: Non-monotonic surface charging phenomena and negative double layer capacitance," *J. Chem. Phys.*, vol. 148, no. 4, Jan. 2018, Art. no. 044704.
[69] T. Pajkossy and D. M. Kolb, "Double layer capacitance of Pt(111) single crystal electrodes," *Electrochimica Acta*, vol. 46, nos. 20–21, pp. 3063–3071, Jul. 2001.
[70] T. Pajkossy and D. M. Kolb, "Double layer capacitance of the platinum group metals in the double layer region," *Electrochemistry Commun.*, vol. 9, no. 5, pp. 1171–1174, May 2007.
[71] K. J. Aoki, "Frequency-dependence of electric double layer capacitance without faradaic reactions," *J. Electroanal. Chem.*, vol. 779, pp. 117–125, Oct. 2016.
[72] K. J. Aoki, J. Chen, X. Zeng, and Z. Wang, "Decrease in the double layer capacitance by faradaic current," *RSC Adv.*, vol. 7, no. 36, pp. 22501–22509, 2017.
[73] U. Kehler, A. Klöhn, O. Heese, and J. Gliemroth, "Hydrocephalus therapy: Reduction of shunt occlusions using a peel-away sheath," *Clin. Neurol. Neurosurgery*, vol. 105, no. 4, pp. 253–255, Sep. 2003.
[74] T. Hudson, A. Baldwin, E. Christian, J. G. McComb, and E. Meng, "Testing a multi-sensor system for hydrocephalus monitoring in external ventricular drains," in *Proc. Int. Conf. Solid-State Sensors, Actuat. Microsyst. Eurosensors*, 2019, p. 4.
[75] R. B. Bird and W. E. Stewart, *Transport Phenomena*. New York, NY, USA: Wiley, 2002.
[76] C. Sosna, T. Walter, and W. Lang, "Response time of thermal flow sensors with air as fluid," *Sens. Actuators A, Phys.*, vol. 172, no. 1, pp. 15–20, Dec. 2011.
[77] A. Baldwin, L. Yu, M. Pratt, K. Scholten, and E. Meng, "Passive, wireless transduction of electrochemical impedance across thin-film microfabricated coils using reflected impedance," *Biomed. Microdevices*, vol. 19, no. 4, p. 11, Dec. 2017, Art. no. 87.
[78] R. Vilares *et al.*, "Fabrication and testing of a SU-8 thermal flow sensor," *Sens. Actuators B, Chem.*, vol. 147, no. 2, pp. 411–417, Jun. 2010.
[79] M. Dijkstra, M. J. de Boer, J. W. Berenschot, T. S. J. Lammerink, R. J. Wiegerink, and M. Elwenspoek, "Miniaturized thermal flow sensor with planar-integrated sensor structures on semicircular surface channels," *Sens. Actuators A, Phys.*, vol. 143, no. 1, pp. 1–6, May 2008.
[80] *LD20-2600B Liquid Flow Sensor*, Sensirion, Stäfa, Switzerland, 2018.
[81] S. Ziegler, R. C. Woodward, H. H.-C. Iu, and L. J. Borle, "Current sensing techniques: A review," *IEEE Sensors J.*, vol. 9, no. 4, pp. 354–376, Apr. 2009.
[82] H. P. Schwan, "Electrode polarization impedance and measurements in biological materials," *Ann. New York Acad. Sci.*, vol. 148, no. 1, pp. 191–209, Feb. 1968.
[83] P. Mirtaheri, S. Grimnes, and O. G. Martinsen, "Electrode polarization impedance in weak NaCl aqueous solutions," *IEEE Trans. Biomed. Eng.*, vol. 52, no. 12, pp. 2093–2099, Dec. 2005.
[84] J. Ortigoza-Diaz, K. Scholten, and E. Meng, "Characterization and modification of adhesion in dry and wet environments in thin-film Parylene systems," *J. Microelectromech. Syst.*, vol. 27, no. 5, pp. 874–885, Oct. 2018.
[85] S. Issa, H. Sturm, and W. Lang, "Modeling of the response time of thermal flow sensors," *Micromachines*, vol. 2, no. 4, pp. 385–393, Oct. 2011.
[86] C. Qin, B. Stamos, and P. K. Dasgupta, "Inline shunt flow monitor for hydrocephalus," *Anal. Chem.*, vol. 89, no. 15, pp. 8170–8176, Aug. 2017.
[87] T. Bork *et al.*, "Development and *in-vitro* characterization of an implantable flow sensing transducer for hydrocephalus," *Biomed. Microdevices*, vol. 12, no. 4, pp. 607–618, Aug. 2010.
[88] R. M. Odland *et al.*, "Efficacy of reductive ventricular osmotherapy in a swine model of traumatic brain injury," *Neurosurgery*, vol. 70, no. 2, pp. 445–455, Feb. 2012.
[89] H. Matsuyama and K. Motoyoshi, "An empirical relation between the limiting ionic molar conductivities and self-diffusion coefficients of pure solvents," *Chem. Phys. Lett.*, vol. 699, pp. 162–166, May 2018.

**Trevor Q. Hudson** (Student Member, IEEE) received the B.S. degree in biomedical engineering from Rice University, in 2014, and the M.S. degree in biomedical engineering from the University of Southern California (USC), in 2016, where he is currently pursuing the Ph.D. degree, also he researches implantable impedimetric sensors and polymer micromachining.

**Ellis Meng** (Fellow, IEEE) received the B.S. degree in engineering and applied science and the M.S. and Ph.D. degrees in electrical engineering from the California Institute of Technology (Caltech), Pasadena, CA, USA, in 1997, 1998, and 2003, respectively. Since 2004, she has been with the University of Southern California, Los Angeles, CA, USA, where she was the Viterbi Early Career Chair and then the Department Chair. She is currently Professor of Biomedical Engineering and holds a joint appointment with the Ming Hsieh Department of Electrical and Computer Engineering. She also serves as the Vice Dean for Technology Innovation and Entrepreneurship. Her research interests include bioMEMS, implantable biomedical microdevices, microfluidics, multimodality integrated microsystems, and packaging. She is a fellow of ASME, BMES, AIMBE, and NAI. She was a recipient of the Intel Women in Science and Engineering Scholarship, the Caltech Alumni Association Donald S. Clark Award, and the Caltech Special Institute Fellowship. She has also received the NSF CAREER and Wallace H. Coulter Foundation Early Career Translational Research Awards. In 2009, she was recognized as one of the TR35 Technology Review Young Innovators under 35.